THE JOURNAL OF PHYSICAL CHEMISTRY C
A JOURNAL OF THE AMERICAN CHEMICAL SOCIETY

Open Access
This article is licensed under CC-BY 4.0

pubs.acs.org/JPCC
Article

Preparation of Porous Al−Cu−Fe−Cr Quasicrystalline Samples by Alkaline Leaching for Adsorption and Catalytic Applications

Miguel L. Laper, Mariana G. Brondi, Manuel Houmard, Augusta Isaac, Eduardo H. M. Nunes, and Witor Wolf*

Cite This: *J. Phys. Chem. C* 2025, 129, 14366−14377

Read Online

ACCESS | Metrics & More | Article Recommendations

ABSTRACT: This study develops a multifunctional porous quasicrystalline (QC) material from an Al−Cu−Fe−Cr alloy for efficient adsorption and catalytic degradation of Congo Red. By optimizing alkaline leaching conditions, the material's porosity, surface chemistry, and functional performance were tailored. An $Al_{85}Cu_6Fe_3Cr_6$ (at%) alloy produced by spray forming was leached in 10 M NaOH for 0.5−48 h to selectively dissolve aluminum and expose active sites. A systematic investigation of the structural evolution and surface properties was conducted, and the adsorption capacity and catalytic behavior of the prepared alloys were also evaluated. After 30 min of controlled leaching, an optimal macroporous structure was produced with 10.9% porosity and a positive surface charge of 7.2 mV. This enhances the electrostatic adsorption of CR, achieving 70% removal within 24 h while maintaining QC phases and accessible active sites. The material also demonstrated effective catalytic activity, achieving complete azo-bond cleavage in under 10 min, favored by oxidized Fe/Cr/Cu species.

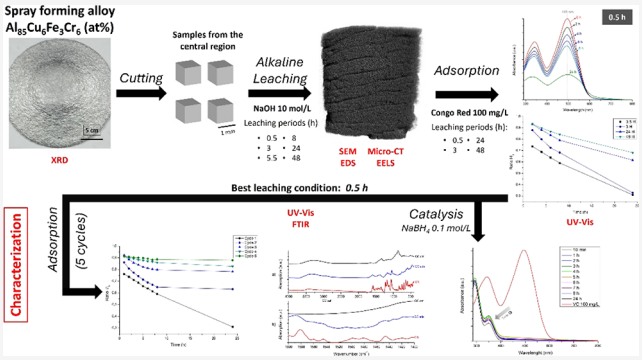

1. INTRODUCTION

Quasicrystals (QCs) are a class of materials that exhibit quasi-periodic translational structures.[1] Since their discovery by Daniel Shechtman,[2] QCs have attracted considerable interest due to their unique structural and physical properties. Over the past four decades, numerous metallic systems have been discovered to form quasicrystalline phases, primarily in aluminum-based binary, ternary, and quaternary alloys. QC phases are generally divided into two categories: metastable and stable phases.[3] The latter can be obtained by conventional melting and solidification processes as they are included in equilibrium phase diagrams. However, the intrinsic brittleness of QCs significantly limits their widespread application in mechanical components.[4] Despite this limitation, certain properties of QCs, such as their high hardness,[5] make them attractive for several applications. For instance, when incorporated into metallic matrices, QCs can act as reinforcing agents, improving the overall performance of materials in various engineering contexts.[6,7]

QCs are also promising in catalysis for several reasons, particularly because they often contain catalytically active elements such as Fe, Pd, Cu and Ni.[8] In addition, their aperiodic yet ordered structure provides a high density of active sites with distinctive electronic and geometric properties that can enhance the adsorption, activation, and desorption of reactants.[9] Quasicrystals also exhibit structural stability at high temperatures and in corrosive environments, making them well suited for demanding processes such as hydrogenation and fuel cell applications.[10,11] Finally, their inherent brittleness favors the production of fine particles by grinding and mechanical milling. Most studies on QCs as catalysts have focused on methanol steam reforming.[12−16] However, their potential applications extend beyond the energy sector. For instance, Mishra et al.[17] investigated the reduction of methylene blue, an organic dye, using the icosahedral phase of the Al−Cu−Fe system. While limited studies have examined the application of porous structures derived from QCs in areas such as hydrogen production and methylene blue degradation,[18,19] there remains a significant gap in research focused on the development of multifunctional porous QC materials capable of functioning as both adsorbents and catalysts for the treatment of organic pollutants, including azo dyes. Moreover, the leaching conditions and their impact on structure, surface charge, and

Received: May 1, 2025
Revised: July 15, 2025
Accepted: July 25, 2025
Published: August 1, 2025

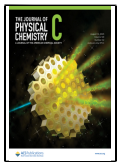

Downloaded via UNIV OF SAO PAULO on September 22, 2025 at 20:06:08 (UTC).
See https://pubs.acs.org/sharingguidelines for options on how to legitimately share published articles.

ACS Publications
© 2025 The Authors. Published by American Chemical Society

https://doi.org/10.1021/acs.jpcc.5c03000
J. Phys. Chem. C 2025, 129, 14366−14377

performance have not been systematically optimized. Recent work by Wolf et al.[20] introduced an Al-rich Al−Cu−Fe−Cr alloy containing stable decagonal QCs and α-Al as primary phases, offering a promising platform for tuning structure and catalytic properties.

In this context, the present study introduces a new one-step alkaline leaching process that modifies the porosity and surface reactivity of $Al_{85}Cu_6Fe_3Cr_6$ alloys. This process eliminates the need for high-temperature post-treatments or the addition of nanoparticles. Our results show that changing the leaching time alters the alloy's microstructure, surface chemistry, and electrostatic properties. These properties enable the alloy to function as both an adsorbent and a catalyst for the removal and degradation of Congo Red (CR), an azo dye frequently used in the textile and paint industries.[21] The sample leached for 30 min exhibited optimal performance due to a synergistic combination of retained quasicrystalline phases, favorable surface charge, and a porous structure. This study integrates phase-engineered QC systems with environmental remediation applications, facilitating the development of reusable, manageable, and multifunctional materials.

2. MATERIALS AND METHODS

2.1. Production of the Al−Cu−Fe−Cr Alloy. A QC-forming alloy with the composition $Al_{85}Cu_6Fe_3Cr_6$ (at%) was used in this study. It was obtained by spray forming. The complete alloy production process required approximately 1 h. This method ensures a homogeneous distribution of the QC phase and other microstructural components,[22] which is critical to achieving the desired properties in the present study. Approximately 2 kg of the alloy was produced per batch by melting commercially pure elements (greater than 99% purity) under an argon atmosphere at 1200 °C. The molten alloy was poured into a preheated alumina funnel where it was atomized using a nitrogen jet (with a nominal atomization pressure of 1 MPa and 99% purity). A 6 mm diameter nozzle was used, and the atomized droplets were deposited on a steel substrate positioned 370 mm from the nozzle. The steel substrate was continuously rotated during the process. The deposit was then cut into cubic samples measuring 10 mm on each side. Samples from the central region of the deposit were used in this study.

2.2. Leaching Step. The cubic samples were leached in an aqueous solution of 10 mol/L sodium hydroxide (NaOH, Synth, ≥ 98%) for periods ranging from 0.5 to 48 h. A volume of 50 mL of alkaline solution was used per gram of material. During leaching, samples were suspended with a nylon cord while the solution was stirred at room temperature. The samples were then rinsed with deionized water and dried in air at 70 °C for 24 h.

2.3. Adsorption and Catalysis. QC samples were immersed and kept for different periods in an aqueous solution containing CR at 100 mg/L. A solution-to-solid ratio of 200 mL per gram of QC was maintained throughout the experiment. At predetermined time intervals between 2 and 24 h, 4 mL aliquots were collected from the solution. The concentration of CR in these aliquots was determined by ultraviolet−visible (UV−vis) spectroscopy using absorption bands at 343 and 496 nm as reference wavelengths. These bands are attributed to π-π^* transitions of the aromatic rings and n-π^* transitions of the electron pairs in the azo bond (—N═N—).[23−26] A linear relationship was observed between absorbance at the most intense band and CR concentration over the range examined. The ratio of the concentrations is equal to the ratio of the absorbance intensities of the two bands, as shown in eq 1. In this equation, $[C_0]$ and $[C_t]$ represent the initial concentration and the concentration at time t, respectively, while I_0 and I_t correspond to the absorbance intensities of the initial solution and the solution at time t. This relationship was used to evaluate the removal of CR from the aqueous solution during the experiments.

$$\frac{[C_t]}{[C_0]} = \frac{I_t}{I_0} \tag{1}$$

The adsorption capacity was determined using UV−vis spectroscopy in accordance with the Beer−Lambert law. First, a calibration curve was constructed using the absorbance of standard CR solutions measured at a wavelength of 496 nm, which corresponds to the maximum absorbance of the dye. Then, the CR concentration was calculated at various time intervals using this curve. Based on the CR concentrations at various time intervals, the removal efficiency (%) was determined using eq 2:

$$\text{Removal Efficiency (\%)} = \left(\frac{C_0 - C_t}{C_0}\right) \times 100\% \tag{2}$$

To evaluate the catalytic potential of the materials, a QC sample leached for 30 min was added to an aqueous CR solution under the same conditions as above. This leaching time was chosen because it seems to optimize the structural properties of the QC alloy used in this study. Sodium borohydride ($NaBH_4$, Aldrich, ≥98%) was then added at a concentration of 0.1 mol/L as a reducing agent. Aliquots were collected at various time intervals and examined by UV−vis spectroscopy.

2.4. Characterization. X-ray diffraction (XRD) was performed on a Philips-PANalytical PW 1710 diffractometer using Cu−Kα radiation (λ = 1.54 Å) and a step size of 0.02 °/s. Samples for scanning electron microscopy (SEM) were prepared using standard metallographic procedures, including embedding in resin, grinding with abrasive papers up to 1200 grit, and polishing with diamond paste. SEM analysis was performed using a Jeol JSM-6360 microscope at an acceleration voltage of 15 kV. Elemental composition was assessed via energy-dispersive spectroscopy (EDS) using a Thermo Noran Quest spectrometer. X-ray microtomography (micro-CT) was performed using a Bruker SkyScan 1174 system at 50 kV, 800 μA, with a 5000 ms exposure time, and a 1.0 mm Al filter. The samples used in these tests were approximately 5 mm thick to ensure that the X-ray photons could penetrate the entire thickness. Metals are known to have a high mass attenuation coefficient (μ/ρ) due to their high density and atomic number.[27] Scans were performed with a pixel size of 10 μm, a 0.7° rotation step, and a full 360° sample rotation. NRecon software was used for three-dimensional image reconstruction.

Fourier transform infrared (FTIR) spectroscopy was conducted using a Bruker Alpha spectrometer at a resolution of 4 cm^{-1} with 128 scans. Measurements were performed in attenuated total reflectance (ATR) mode, using a diamond crystal as the reflecting element. UV−vis spectroscopy was performed using a Shimadzu UV-2600 spectrophotometer with a resolution of 0.5 cm^{-1} and a slow scan speed over the spectral range of 280−800 nm, with deionized water as the reference. Transmission electron microscopy (TEM) was performed on a

https://doi.org/10.1021/acs.jpcc.5c03000
J. Phys. Chem. C 2025, 129, 14366−14377

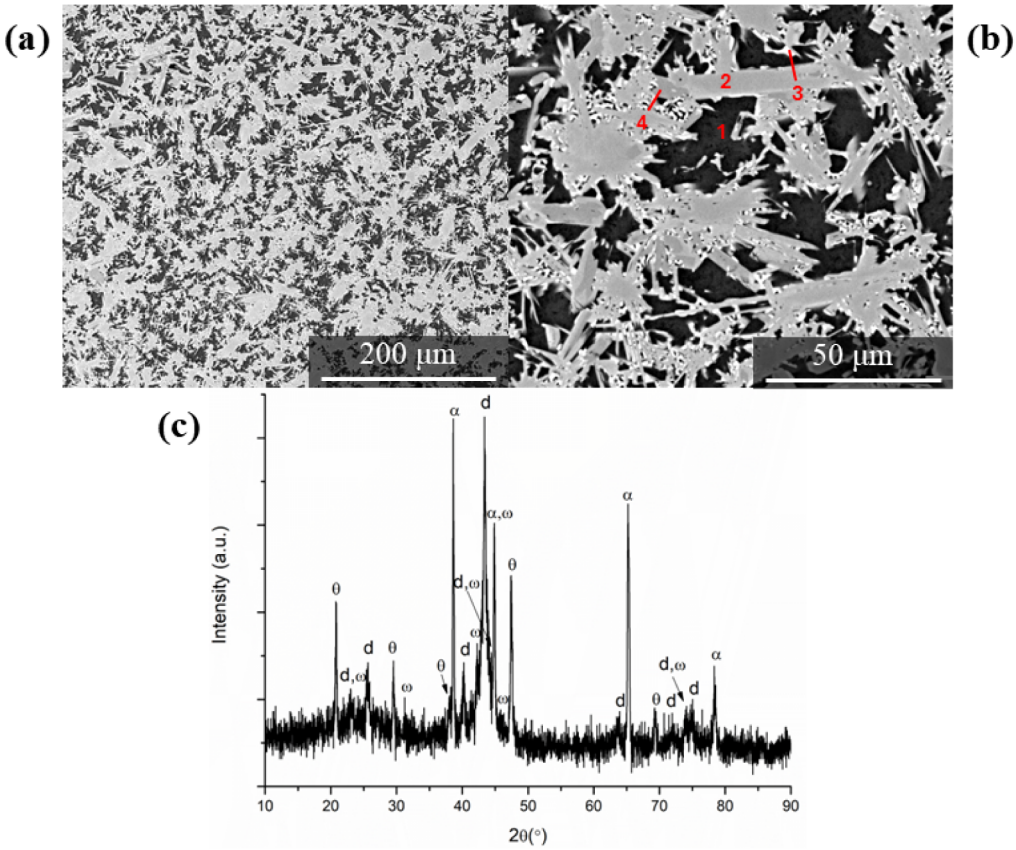

Figure 1. (a,b) SEM micrographs of the spray-formed alloy, with scale bars corresponding to 200 and 50 μm, respectively. SEM images were obtained using secondary electron signals. (c) Typical XRD pattern of the QC alloy.

Tecnai G2−20 FEI SuperTwin microscope at an acceleration voltage of 200 kV. The system was equipped with a Gatan Quantum electron energy loss spectroscopy (EELS) detector and an Oxford Instruments EDS system. TEM samples were prepared from the QC material leached for 30 min in a 10 mol/L NaOH solution. Particles were removed from the sample surface by mechanical grinding, then sonicated in isopropyl alcohol for 20 min at room temperature before depositing on a copper grid for TEM analysis. EELS data were acquired in the 475−985 eV range with an energy resolution of 1.8 eV and processed using DigitalMicrograph software.

Zeta potential measurements were carried out using a ZetaPALS analyzer (Brookhaven Instruments Corporation) with Zeta Potential Analyzer software (version 5.59). For sample preparation, the leached region was mechanically removed, milled, and suspended in deionized water. High-Resolution Micro-CT imaging was performed on as-cast samples, as well as on samples leached for 30 min and 48 h, to evaluate pore evolution. Rectangular specimens measuring 10 mm in height and approximately 2.5 mm by 2.5 mm in cross-section were scanned using a ZEISS Xradia Context micro-CT scanner operated at 140 kV and 150 μA, with a 0.225° rotation step, an exposure time of 0.6 ms, and a voxel resolution of 3.14 μm. Image reconstruction was performed using the Reconstructor 16.1 Control System, and porosity quantification was conducted with Avizo Thermo Fisher 2023 software.

3. RESULTS AND DISCUSSION

3.1. Spray-Formed Alloy. Figure 1a,b shows SEM micrographs of the spray-formed deposit. These images reveal three distinct microstructural features: (i) equiaxed or rod-like particles corresponding to the decagonal quasicrystalline (d-QC) phase, (ii) a dark gray matrix, identified as the α-Al (aluminum-rich) solid solution, and (iii) bright white regions attributed to intermetallic phases, primarily θ-Al_2Cu and ω-Al_7Cu_2Fe. These phase identifications are consistent with the energy-dispersive spectroscopy (EDS) results (Table 1) and with the detailed characterizations of this alloy system reported by Wolf et al.[28] That study provides comprehensive structural information, including electron diffraction data confirming the decagonal symmetry of the QC phase and the distinct morphologies of each constituent phase. SEM micrographs show that the spray forming process yields a refined, multiphase microstructure, featuring well-dispersed quasicrystalline and intermetallic phases embedded within an aluminum

Table 1. Chemical Composition and Crystalline Phases Identified in the Highlighted Regions of Figure 1b

Region	Phase	Element(at%)			
		Al	Cu	Fe	Cr
1	α	97.4	1.9	0.2	0.5
2	d	79.9	3.7	5.3	11.1
3	Mixture of phases	75.4	21.6	1.0	2.0
4	d	79.9	2.3	4.4	13.4

https://doi.org/10.1021/acs.jpcc.5c03000
J. Phys. Chem. C 2025, 129, 14366−14377

matrix. This matrix serves as the precursor to the porous material produced by alkaline leaching in the present study.

3.2. Alkaline Attack. Surfaces were flat and smooth after cutting. After alkaline treatment with NaOH, significant changes in surface morphology were observed, with the treated samples showing increased roughness and a darker coloration. To further investigate these changes, a sample treated for 48 h was examined by micro-CT (Figure 2). This analysis revealed a significant increase in surface roughness and porosity throughout the sample. These morphological changes are attributed to the selective leaching of Al from the QC-based alloy during the alkaline treatment, which is likely to create microscale voids in the alloy, thereby increasing the overall surface area.[19] These results highlight the reactivity of QC alloys under alkaline conditions and may have implications for applications where surface properties, such as catalytic activity, are critical.

Figure 2. Micro-CT image of the QC sample leached in NaOH alkaline solution for 48 h. The scale bar represents 5 mm.

SEM images of samples exposed to leaching for different durations are shown in Figure 3, while the average depth of chemical attack as a function of leaching time is given in Table 2. The results reveal a clear correlation between leaching duration and the extent of surface alteration, with longer exposure leading to progressively deeper chemical attack. The progressive dissolution of aluminum over time indicates a time-dependent reaction, in which the alkaline medium gradually penetrates the matrix. This results in controlled etching, followed by accelerated degradation. As shown in Figure 3, the leached region has a distinct two-layer structure: "Region 1", a darker area near the surface, and "Region 2", a lighter zone between "Region 1" and the unaffected matrix. Both regions are marked in Figure 3.

Table 2. Depth of Chemical Attack at Different Leaching Times

Leaching time (h)	Depth (μm)
0.5	37.8 ± 9.1
3.0	111.4 ± 8.8
5.5	153.1 ± 10.2
8.0	155.1 ± 11.0
24	252.3 ± 15.3
48	376.4 ± 40.0

To further investigate the chemical differences between these regions, EDS measurements were performed. The atomic compositions of "Region 1" and "Region 2" are shown in Figure 4, and their average chemical compositions are summarized in Table 3. These results represent the average compositions across several samples leached for 3 h or longer; for the sample leached for 0.5 h, only Region 1 was present and analyzed. This identification was based on two key observations: (i) the absence of a distinct tonal or compositional contrast, which distinguishes two separate regions in samples with longer leaching times, and (ii) the close similarity of its elemental composition to that of Region 1 in the other samples. During alkaline leaching, two chemically distinct regions form: Region 1 near the surface and Region 2 beneath it. This occurs due to the alloy's heterogeneous microstructure and the preferential dissolution of aluminum in the sodium hydroxide solution. The α-Al phase, which is aluminum-rich, is significantly more reactive and dissolves more readily than the surrounding quasicrystalline and intermetallic phases. This leads to the development of an outer layer (Region 1) that is

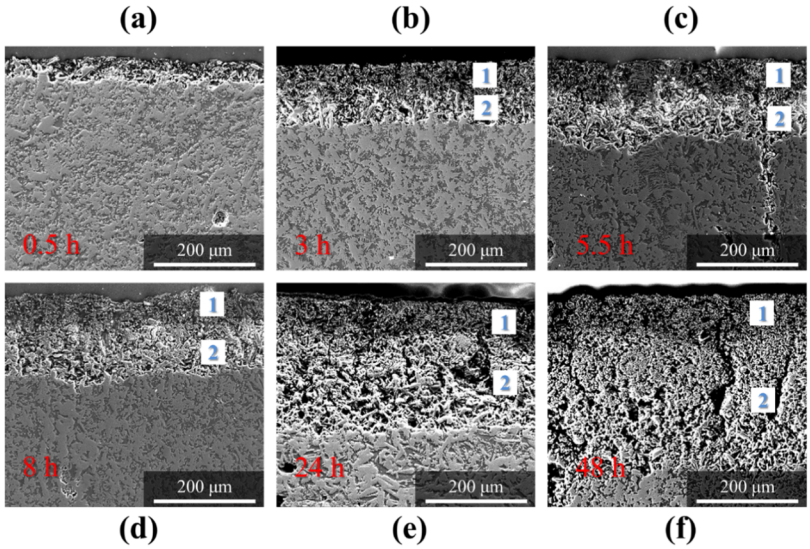

Figure 3. SEM secondary electron micrographs of the leached samples after (a) 0.5 h, (b) 3.0 h, (c) 5.5 h, (d) 8.0 h, (e) 24 h, and (f) 48 h. The scale bars indicate 200 μm.

https://doi.org/10.1021/acs.jpcc.5c03000
J. Phys. Chem. C 2025, 129, 14366−14377

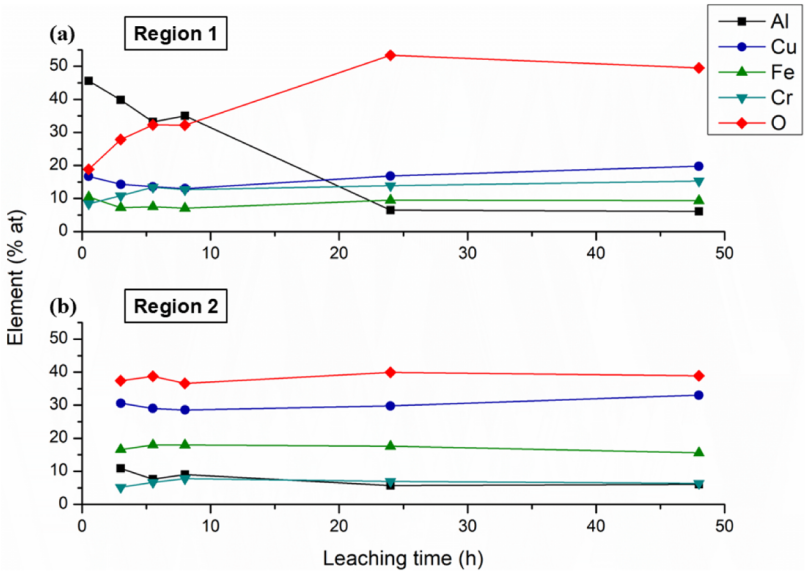

Figure 4. Chemical composition of (a) Region 1 (near the surface) and (b) Region 2 (located between Region 1 and the unaffected matrix).

Table 3. Average Chemical Composition (at%) of Region 1 and Region 2 in the Leached Samples

	Al	Cu	Fe	Cr	O
Region 1	7.9 ± 2.2	30.2 ± 1.8	17.1 ± 1.0	6.6 ± 1.0	38.3 ± 1.3
Region 2	27.7 ± 17.1	15.7 ± 2.5	8.5 ± 1.4	12.4 ± 2.4	35.7 ± 13.2

highly modified, exhibiting increased porosity and elevated oxygen content due to the formation of oxides and hydroxides of Al, Cu, Fe, and Cr. As leaching progresses, the alkaline solution gradually penetrates deeper, reacting with subsurface aluminum-rich zones and forming Region 2. Although Region 2 is affected by the leaching process, it generally retains more of the original microstructure and displays lower porosity and oxidation levels than Region 1. This clear distinction between the two layers highlights the diffusion-limited and composition-dependent nature of the alkaline leaching mechanism.

In addition to inducing morphological changes, alkaline leaching significantly affected the porosity of the samples. As shown in Table 4, the total porosity increased from 7.2% in the as-cast condition to 10.9% after 0.5 h of leaching, and further to 36.2% after 48 h. This increase confirms that the leaching process generates voids by selectively dissolving aluminum-rich phases, particularly near the surface. As expected, High-Resolution micro-CT analysis revealed that surface porosity increased with longer leaching times. The sample leached for 48 h exhibited substantially higher surface porosity than the sample leached for only 0.5 h, due to extended exposure to the alkaline solution, which promotes deeper aluminum dissolution and the formation of surface pores. Although large pores (up to 105 μm) were detected in all samples, they were extremely rare, representing less than 0.1% of the total pore population. In contrast, more than 93% of the pores had diameters smaller than 20 μm. These findings demonstrate that alkaline leaching not only increases overall porosity but also modifies the internal pore structure in a time-dependent manner.

Table 4. Micro-CT Quantification of Porosity and Pore Size in As-Cast and Leached Samples

Sample condition	Total porosity (%)	Average pore size (μm)
As Cast	7.2	6.91 ± 8.11
0.5 h Leached	10.9	9.97 ± 10.77
48 h Leached	36.2	7.49 ± 5.7

Further XRD analyses were conducted on the leached samples to investigate the structural evolution during alkaline treatment. The XRD pattern of the sample leached for 30 min (Figure 5) shows that the characteristic peaks of the decagonal quasicrystalline phase are visible, confirming the remarkable stability of this phase under the applied leaching conditions. In contrast, the peaks corresponding to the α-Al phase and the other intermetallic phases that were prominent in the as-cast sample were significantly reduced or completely absent after leaching. This finding supports the conclusion that aluminum-rich phases dissolve more rapidly in the early stages of alkaline leaching. Additionally, the formation of various oxides and hydroxides of the constituent elements (Al, Cu, Fe, and Cr) was indicated by the appearance of broader peaks.

The XRD pattern of the sample leached for 48 h (Figure 5) showed an absence of all peaks associated with the original decagonal QC phase or any remaining metallic phases. Instead, only peaks associated with the oxides and hydroxides of Al, Cu, Fe, and Cr were detected. This behavior shows that prolonged exposure to an alkaline environment causes extensive structural changes and the formation of a dense oxide/hydroxide layer. As previously discussed, it is believed that this dense surface layer blocks active catalytic and adsorption sites. This explains the observed decline in performance over extended leaching times.

The results in Figure 4 and Table 3 indicate a significant increase in oxygen levels within the attacked regions. This behavior can be attributed to the fact that leaching is an oxidation process that occurs in two stages: (i) the chemisorption of oxygen and (ii) the formation of a thin oxide layer on the surface.[19] Aluminum was reported to have a

https://doi.org/10.1021/acs.jpcc.5c03000
J. Phys. Chem. C 2025, 129, 14366−14377

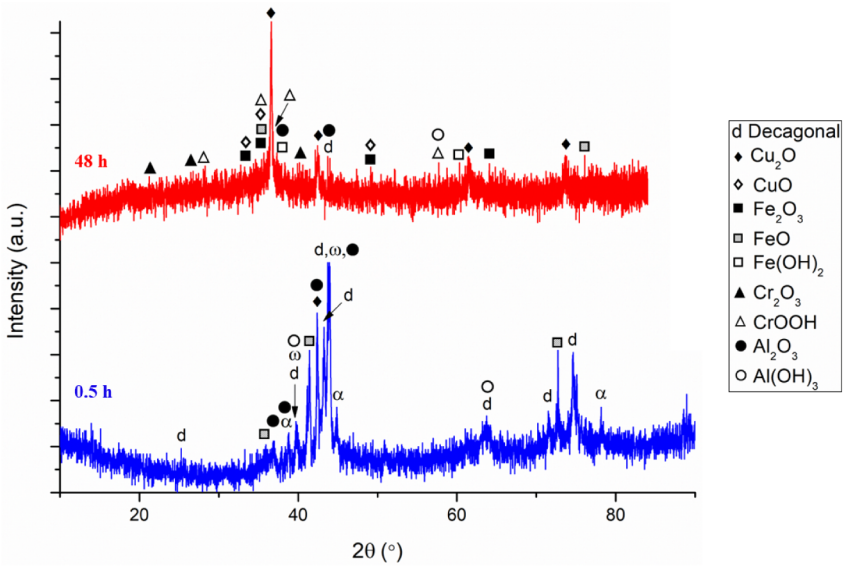

Figure 5. XRD pattern of the samples leached for 30 min (blue) and 48 h (red).

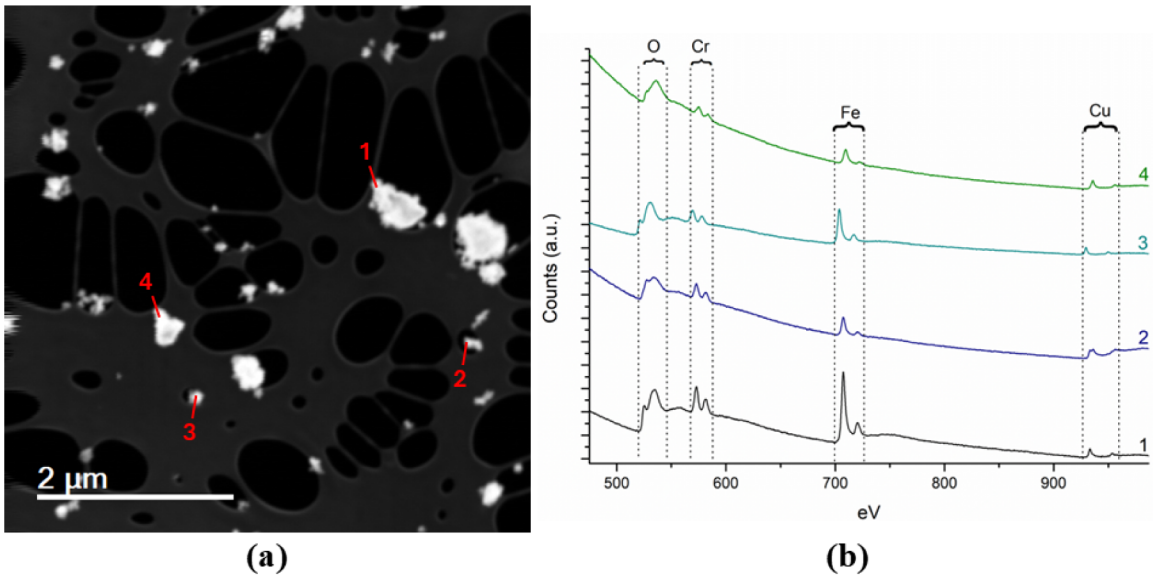

Figure 6. (a) TEM dark-field image of the powdered sample obtained from the alloy leached for 30 min; (b) EELS spectra of the particles highlighted in (a).

relatively high dissolution rate compared to other elements in a study by Mishra et al.[29] on an Al−Cu−Fe alloy. Similarly, Ura-Binczyk et al.[30] observed this phenomenon in Al−Cr−Fe and Al−Cu−Fe−Cr alloys. Yadav et al.[31] investigated the effects of NaOH leaching on quasicrystalline Al−Cu−Fe samples and reported that washing the leached surfaces with methanol and water effectively removed most of the alumina (Al_2O_3) precipitates. These results corroborate previously reported results in the literature and are consistent with the drastic reduction in Al levels observed in Figure 4 and Table 3.

EELS have been used to identify the chemical elements that underwent reactions with NaOH during the leaching process. Figure 6a displays the analyzed region, observed in dark-field mode using a TEM setup. Four different particles, removed from the leached region, were selected for detailed examination using both EDS and EELS analysis, as shown in Figure 6a. The EDS results confirmed the presence of Al, Fe, Cr, and O in all analyzed particles. It should be noted that the sample was mounted on a Cu grid for TEM analysis; however, Cu signals were excluded from the EDS results to prevent interference and ensure an accurate interpretation of the sample's intrinsic composition. Figure 6b presents the EELS spectra corresponding to the particles highlighted in Figure 6a. The spectra reveal uniform chemical behavior, exhibiting consistent features across all analyzed regions. The energy loss peak at 532 eV suggests the presence of O^{2-},[32−34] indicating the formation of oxide species during the leaching process. The peaks at 575 and 584 eV are attributed to Cr^{3+}, confirming the oxidation of chromium to its trivalent state.[34,35] Similarly, the peaks at 708 and 721 eV are characteristic of Fe^{3+}, indicating the oxidation of iron to its trivalent form.[35−37] The peaks at 931 and 951 eV further support the presence of Cu^{+}/Cu^{2+}, reinforcing the oxidation of copper.[35,38−40]

https://doi.org/10.1021/acs.jpcc.5c03000
J. Phys. Chem. C 2025, 129, 14366−14377

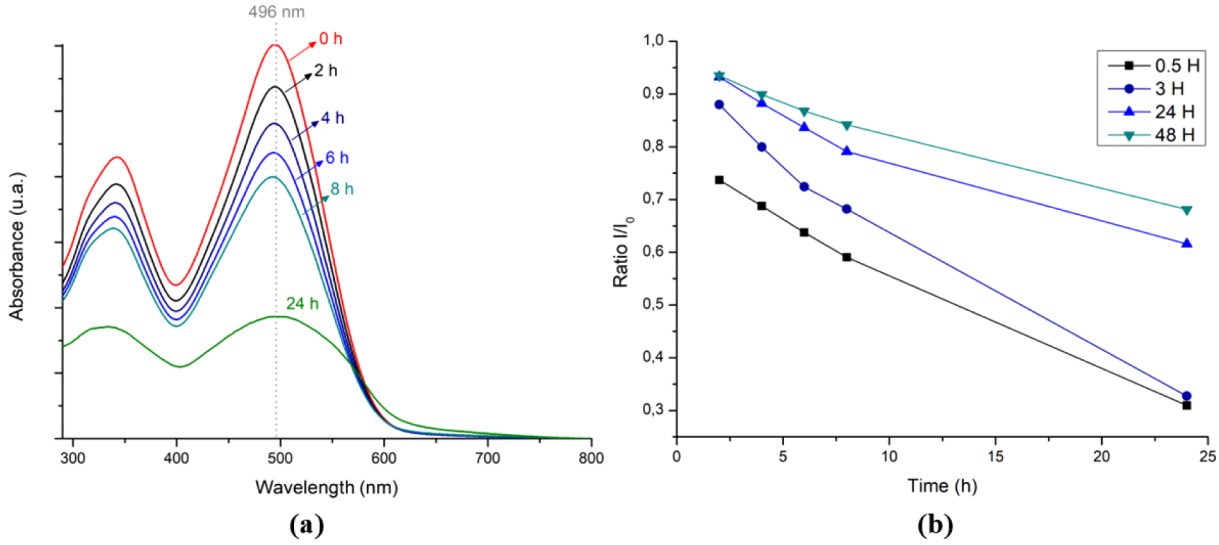

Figure 7. (a) UV−vis spectra of aliquots taken at different time intervals from the CR solution with the sample leached in alkaline solution for 30 min. (b) I_t/I_0 ratio in the region around 496 nm for samples leached for 0.5, 3, 24, and 48 h at different time intervals.

Notably, in the EELS analysis, the energy loss regions associated with Al fall outside the spectral range examined, preventing the direct detection of Al-related transitions in this study. However, the presence of Al in the EDS results, combined with the observed oxidation of Fe, Cu and Cr, strongly suggests that all metallic elements in the alloy reacted with NaOH during leaching. This reaction likely resulted in the dissolution of Al and the formation of oxidized Fe, Cu and Cr species, which are known to contribute to the formation of active catalytic sites.[17] These results provide critical insights into the chemical transformations that occur during alkaline leaching. The oxidation of Fe, Cu and Cr, coupled with the inferred dissolution of Al, highlights the complex interplay between the alloying constituents and the alkaline environment. The resulting surface modifications, including the formation of oxide species and the exposure of active sites, are likely responsible for the improved catalytic properties observed in the leached material, as shown below. This highlights the potential of alkaline leaching as a method of tailoring the surface chemistry of QC alloys.

Leaching has been reported to be an efficient method for the creation of a porous metallic structure and the exposure of sites on the surface of metal alloys,[18,19,29] In the case of the QC alloy studied here, alkaline attack also causes the formation of macropores (i.e., pores larger than 50 nm.[41] As mentioned above, the main phases present in the microstructure of this material are α-Al, decagonal quasicrystals (d-QC) and intermetallic compounds (θ and ω). The leaching step removes aluminum from these phases, with the α-Al phase—composed primarily of aluminum—being the major component removed from the structure. As a result, the remaining "skeleton" in the affected region consists primarily of intermetallic compounds and the QC phase.

3.3. Adsorption and Catalysis. Figure 7a shows the UV−vis spectra obtained at different time intervals of contact with the CR solution, for a QC-based sample leached in NaOH for 30 min. The absorption bands of CR decrease significantly upon interaction with the leached sample, accompanied by slight shifts (around 2 nm) to lower wavelengths. Kamal et al.[42] reported a similar behavior in a study of CR degradation, attributing this shift to the adsorption of CR on copper nanoparticles incorporated into a chitosan matrix. The results for the sample leached for 30 min are consistent with those of the other samples leached for longer periods. The main difference is that the sample leached for 30 min displayed a higher adsorption capacity. As previously mentioned, the adsorption capacity of the samples was evaluated using the ratio between the absorbance intensities of these two bands, as expressed in eq 1. Figure 7b shows this ratio for samples leached in NaOH for different times. It can be observed that, at shorter leaching times, the CR concentrations in solution were lower over the same period, indicating a higher adsorption capacity of the samples. Two control systems were also examined, (i) a CR solution with no sample and (ii) a CR solution with an unleached QC sample. In both cases, compared to the original solution, no significant change in the intensity of the absorption bands was observed. These results emphasize the necessity of leaching the QC samples to adsorb the dye. It is important to note that, since no significant shift was observed in the bands at 343 and 496 nm, the process can be attributed to adsorption rather than catalytic degradation of CR. After 24 h of immersion in CR solutions, all samples showed small CR crystals on their surfaces.

The sample leached for 0.5 h was the most effective among the conditions studied (Figure 7b), reaching a CR removal efficiency of about 70%, after 24 h of immersion. Although the adsorption capacities of the samples leached for 0.5 and 3 h are similar, the sample leached for 3 h experienced a longer and more complex chemical attack. From an optimization point of view, the sample leached for a shorter time (0.5 h) is preferred. Therefore, this condition was selected for the subsequent adsorption cycling tests. The superior adsorption performance of the 0.5 h leached sample can be attributed to two main factors: favorable surface charge characteristics and preservation of active phases after leaching, as confirmed by zeta potential measurements and XRD analysis, respectively. The measured zeta potential values at pH 7 were: CR solution, (−36.76 ± 4.1) mV; sample leached for 30 min, (+7.2 ± 4.2) mV; and sample leached for 48 h, (−24.4 ± 5.0) mV. These results indicate that CR is an anionic dye and is therefore electrostatically attracted to positively charged surfaces. The sample leached for 30 min exhibits a slightly positive surface

https://doi.org/10.1021/acs.jpcc.5c03000
J. Phys. Chem. C 2025, 129, 14366−14377

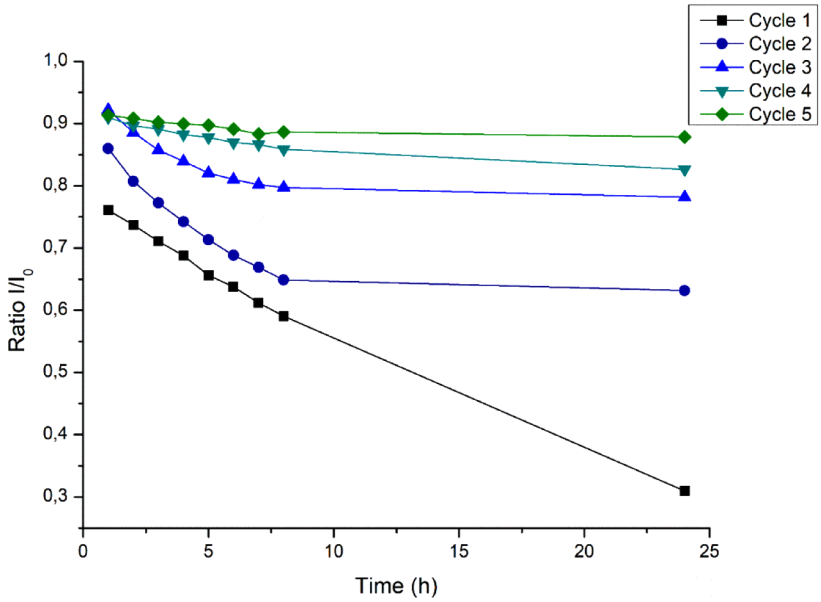

Figure 8. Ratio between I_t and I_0 for each adsorption cycle for the sample leached in an alkaline solution for 0.5 h.

charge, which promotes favorable electrostatic interactions with CR molecules, enhancing adsorption efficiency. In contrast, the sample leached for 48 h has a strong negative surface charge. This charge repels the anionic dye, reducing adsorption performance by inhibiting interaction between pollutant molecules and adsorption sites.

This decline in adsorption capacity with longer leaching times is further explained by the phase evolution revealed in the XRD patterns. The sample leached for 30 min retains the decagonal quasicrystalline phase along with some residual intermetallic phases, which, although partially transformed, continue to provide active sites for adsorption. However, after 48 h of leaching, XRD analysis shows that all original crystalline phases have been replaced by a mixture of oxides and hydroxides of Al, Cu, Fe, and Cr. This indicates the formation of a thick, dense passivation layer that not only alters the surface charge (as reflected by the negative zeta potential) but also likely blocks access to catalytic and adsorption sites. Consequently, prolonged leaching results in both an unfavorable surface charge and physical obstruction of active regions, leading to the observed decrease in adsorption efficiency. The adsorption of CR by the porous QC alloy is therefore understood as a complex and multimechanism process involving several important interactions, including electrostatic attraction and/or anion exchange,[43] hydrogen bonding,[44] surface complexation or chemical bonding,[45] and pore filling.[46]

The cycling tests followed the same time intervals for collecting aliquots of the CR solution. Five cycles were performed to assess the effectiveness of the material on the adsorption of the CR. Before each cycle, the QC-based alloy was washed with deionized water. Figure 8 depicts the absorbance ratio for the sample leached for 0.5 h over time during five adsorption cycles. As observed, the concentration of CR in the solution decreases over time in all cycles, indicating increased adsorption of the dye to the material surface. Importantly, in all the collected aliquots, the position of the absorption bands at 343 and 496 nm did not change significantly. This suggests that the process involves adsorption exclusively, rather than catalysis. However, the I_t/I_0 ratio increased in subsequent cycles for each period analyzed. This behavior suggests that the adsorption capacity of the material decreases after immersion in the CR solution and subsequent washing with deionized water. It can be concluded that some active sites remain occupied by CR molecules even after washing, indicating that the cleaning process does not completely regenerate the material.

The potential of the QC samples as catalysts was also evaluated. Figure 9 displays the UV−vis spectra of aliquots collected at various time intervals. In these tests, the sample leached for 30 min was immersed in a solution of CR and $NaBH_4$.

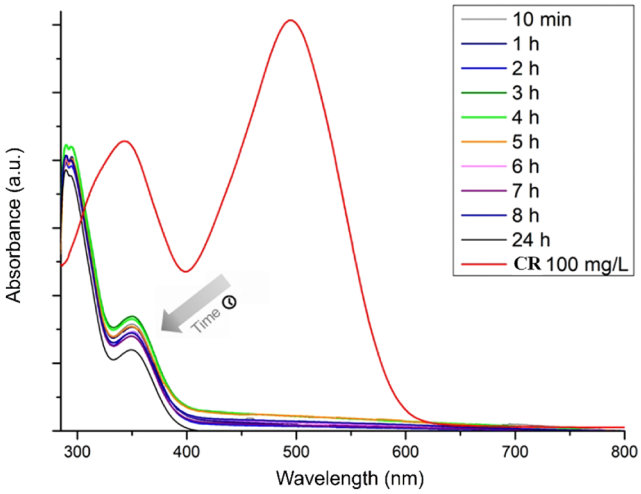

Figure 9. UV−vis spectra of aliquots taken at different times from the CR and $NaBH_4$ solution in which the QC was leached for 30 min.

As observed, the characteristic absorption peaks of CR at 343 and 496 nm either disappeared or shifted to lower wavelengths after immersion times as short as 10 min. All aliquots collected showed absorption peaks at about 290 and 350 nm. The changes in the UV−vis spectrum indicate that the original CR molecules were broken down into smaller

https://doi.org/10.1021/acs.jpcc.5c03000
J. Phys. Chem. C 2025, 129, 14366−14377

fragments during the catalytic process.[42,47−51] Notably, no significant changes were detected in aliquots taken from CR and $NaBH_4$ solutions without the QC leached sample (Figure 10).

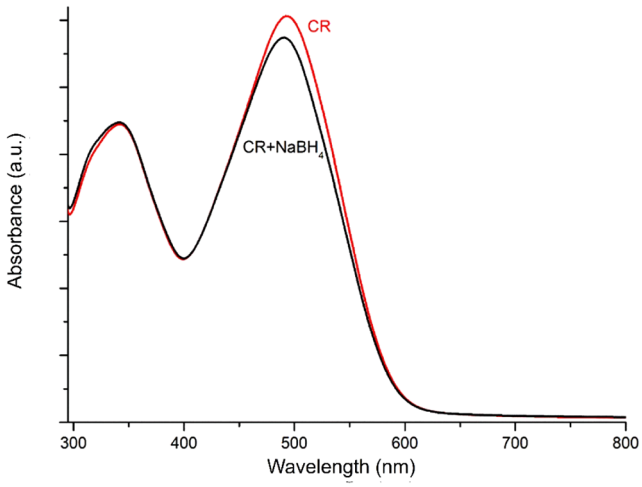

Figure 10. UV−vis spectra of an aqueous CR solution before and after the addition of the reducing agent ($NaBH_4$). Notably, the QC sample was not present in this solution.

The solution's color changed from deep red to colorless with the QC sample, indicating CR degradation. Based on these observations, we conclude that the QC samples act as catalysts, accelerating the chemical reaction between $NaBH_4$ and the azo bonds.[42,47−52] This conclusion is further supported by the FTIR results shown in Figure 11. Figure 11a shows the spectra of three samples: CR powder, the QC sample after adsorption of CR (QC-ads), and the sample that catalyzed the degradation of CR in the presence of a reducing agent (QC-cat). Many of the absorption bands observed in the FTIR spectrum of CR are also present in the spectrum of QC ads. This indicates that no significant chemical changes have occurred in the molecular structure of CR, which remained in solution after partial adsorption by the leached QC sample. However, the spectrum of QC-cat is significantly different from the others. Figure 11b shows a zoomed view of the spectral range of 1600−1400 cm^{-1}. In this region, two absorption bands appear in the spectra of CR and QC-ads but are absent in the spectrum of QC-cat. These bands, located at about 1590 cm^{-1} and 1447 cm^{-1}, have been related to the stretching mode of azo bonds.[53,54]

In this study, the catalytic degradation of CR by $NaBH_4$ in the presence of leached QC alloy was investigated to assess its potential as a catalyst for azo dye reduction. CR is a toxic anionic dye, characterized by azo bonds (—N═N—) that are resistant to spontaneous reduction in aqueous environments. Although $NaBH_4$ is a strong reducing agent, the reduction of CR is thermodynamically favorable but kinetically limited in the absence of a catalyst, primarily due to electrostatic repulsion between the negatively charged BH_4^- ions and the sulfonate groups of CR.[55,56] In this study, the leached QC alloy acted as an efficient catalyst, facilitating the electron transfer from BH_4 ions to CR molecules. The reaction progress was monitored by UV−vis spectroscopy. This revealed a rapid disappearance of the characteristic absorption peaks of CR at 343 and 496 nm, both associated with its azo bonds, accompanied by a visible color change from deep red to colorless. This spectral behavior indicates cleavage of the azo bonds and subsequent formation of smaller aromatic amines, consistent with observations reported for similar catalytic systems. In contrast, control experiments conducted without the catalyst (CR only) showed negligible spectral changes, further confirming the catalytic activity of the leached QC alloy (Figure 10).

The degradation mechanism of CR involves three main steps: (i) adsorption of CR and BH_4^- ions onto the catalyst surface, (ii) electron transfer from BH_4^- to CR, and (iii) desorption of the resulting degradation products.[23] The porous structure of the leached QC alloy, enriched with oxidized Fe, Cu and Cr species (Section 3.2), provides abundant active sites for both adsorption and electron transfer. In support of this mechanism, the FTIR spectrum of the catalyst after the reaction (QC-cat, Figure 11) shows the disappearance of peaks at 1590 cm^{-1} and 1447 cm^{-1}, corresponding to azo bond

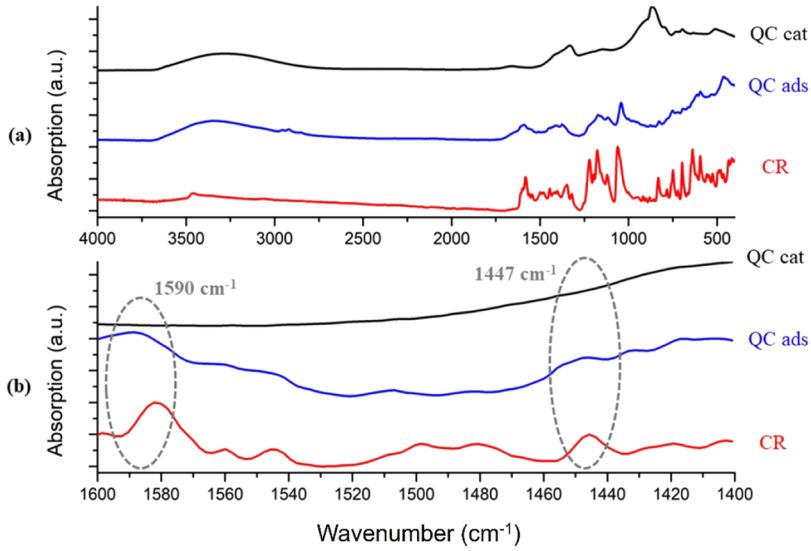

Figure 11. FTIR spectra of pure CR, QC after partial adsorption of CR, and QC after catalysis of CR. (a) Spectra from 4000 cm^{-1} to 400 cm^{-1}, while (b) focus on the region from 1600 cm^{-1} to 1400 cm^{-1}.

https://doi.org/10.1021/acs.jpcc.5c03000
J. Phys. Chem. C 2025, 129, 14366−14377

stretching vibrations, confirming the cleavage of these bonds. This observation is consistent with previous reports in which metal nanoparticles (e.g., Ag, Au) act as electron mediators, favoring azo bond weakening through conjugation and hydrogenation.[57,58] The QC alloy offers advantages over conventional nanoparticle-based catalysts, such as ease of recovery and reuse without the need for stabilizing matrices (e.g., polymers or ceramics). Its native form eliminates complications like nanoparticle leakage, a common issue in dispersed systems.[50] Moreover, the leaching step tailors the surface chemistry, enhancing catalytic activity through selective Al dissolution and exposure of redox-active Fe/Cr species. This catalytic efficiency is attributed to the unique microstructure of the QC alloy and the synergistic interactions between its constituent phases. In future studies, parameters such as catalyst dosage, $NaBH_4$ concentration and pH may be optimized for further performance improvement.

4. CONCLUSIONS

This study demonstrates for the first time the preparation of porous quasicrystalline samples in the Al−Cu−Fe−Cr system via alkaline leaching with NaOH, using an $Al_{85}Cu_6Fe_3Cr_6$ (at %) alloy produced by spray forming. The as-cast alloy contained α-Al, a stable decagonal quasicrystalline phase, and copper-rich intermetallics (θ-Al_2Cu and ω-Al_7Cu_2Fe). Controlled leaching selectively dissolved the aluminum-rich α-Al phase, creating a porous structure that exposed active catalytic sites composed of Cu, Fe, and Cr, thereby enhancing the surface reactivity. Adsorption tests with CR, a hazardous dye of great concern, confirmed that the leaching step significantly affects performance. A sample leached for 30 min retained the QC phase and an optimal surface charge of +7.2 mV, which favors electrostatic attraction to the anionic dye (−36.76 mV). However, leaching for 48 h produced a dense oxide layer and a negative surface charge of −24.4 mV. These changes resulted in reduced adsorption efficiency due to site blockage and electrostatic repulsion. The 30 min leached sample maintained adsorption capacity over several reuse cycles and also acted as an effective catalyst, achieving complete azo bond cleavage within 10 min in the presence of $NaBH_4$. Notably, the leached samples are bulk macroscopic solids that can be easily handled and recovered without filtration or centrifugation, offering practical advantages for real-world applications. Together, the dual adsorption-catalytic functionality, reusability, and simple processing highlight the potential of leached Al−Cu−Fe−Cr quasicrystalline materials as promising candidates for scalable industrial wastewater treatment.

■ AUTHOR INFORMATION

Corresponding Author

Witor Wolf − *Departamento de Engenharia de Materiais, Escola de Engenharia de São Carlos, Universidade de São Paulo, São Carlos, SP CEP: 13566-590, Brasil;* orcid.org/0000-0002-8919-140X; Email: witorw@usp.br

Authors

Miguel L. Laper − *Programa de Pós-Graduação em Engenharia Metalúrgica, Materiais e de Minas, Universidade Federal de Minas Gerais, Belo Horizonte, MG CEP: 31270-901, Brasil*

Mariana G. Brondi − *Programa de Pós-Graduação em Engenharia Metalúrgica, Materiais e de Minas and Programa de Pós-Graduação em Engenharia Química, Universidade Federal de Minas Gerais, Belo Horizonte, MG CEP: 31270-901, Brasil;* orcid.org/0000-0002-2228-8960

Manuel Houmard − *Departamento de Engenharia Química, Universidade Federal de Minas Gerais, Belo Horizonte, MG CEP: 31270-901, Brasil;* orcid.org/0000-0002-1543-5416

Augusta Isaac − *Departamento de Engenharia Metalúrgica e de Materiais, Universidade Federal de Minas Gerais, Belo Horizonte, MG CEP: 31270-901, Brasil;* orcid.org/0000-0001-8617-0956

Eduardo H. M. Nunes − *Departamento de Engenharia Metalúrgica e de Materiais, Universidade Federal de Minas Gerais, Belo Horizonte, MG CEP: 31270-901, Brasil;* orcid.org/0000-0001-6653-5137

Complete contact information is available at: https://pubs.acs.org/10.1021/acs.jpcc.5c03000

Funding

The Article Processing Charge for the publication of this research was funded by the Coordenacao de Aperfeicoamento de Pessoal de Nivel Superior (CAPES), Brazil (ROR identifier: 00x0ma614).

Notes

The authors declare no competing financial interest.

■ ACKNOWLEDGMENTS

The authors acknowledge the financial support of FAPEMIG (APQ-00762-21 and APQ-00792-17), CNPq (306193/2020-5, 403191/2021-1, and 304415/2021-9), FAPESP, and CAPES (PROEX). The authors also acknowledge the technical support provided by UFMG and UFSCar. Special thanks are given to Prof. Guilherme Zepon of UFSCar for providing the Al−Cu−Fe−Cr alloy used herein. W.W. would like to acknowledge the University of São Paulo for the financial support through the announcement for new faculty members (process number 22.1.09345.01.2).

■ REFERENCES

(1) Levine, D.; Steinhardt, P. J. Quasicrystals, I. Definition and Structure. *Phys. Rev. B* **1986**, *34* (2), 596.

(2) Shechtman, D.; Blech, I.; Gratias, D.; Cahn, J. W. Metallic Phase with Long-Range Orientational Order and No Translational Symmetry. *Phys. Rev. Lett.* **1984**, *53*, 1951−1953.

(3) Wolf, W.; Bolfarini, C.; Kiminami, C. S.; Botta, W. J. Recent Developments on Fabrication of Al-Matrix Composites Reinforced with Quasicrystals: From Metastable to Conventional Processing. *J. Mater. Res.* **2020**, *35*, 1−17.

(4) Dubois, J.-M. Potential and Marketed Applications of Quasicrystalline Alloys at Room Temperature or Above. *Rend. Lincei Sci. Fis. Nat.* **2023**, *34*, 689−702.

(5) Wolf, W.; Schulz, R.; Savoie, S.; Bolfarini, C.; Kiminami, C. S.; Botta, W. J. Structural, Mechanical and Thermal Characterization of an Al-Co-Fe-Cr Alloy for Wear and Thermal Barrier Coating Applications. *Surf. Coat. Technol.* **2017**, *319*, 241−248.

(6) Wolf, W.; Aliaga, L. C. R.; Travessa, D. N.; Afonso, C. R. M.; Bolfarini, C.; Kiminami, C. S.; Botta, W. J. Enhancement of Mechanical Properties of Aluminum and 2124 Aluminum Alloy by the Addition of Quasicrystalline Phases. *Mater. Res.* **2016**, *19*, 74−79.

(7) Li, R. T.; Wang, Z. Y.; Sun, W.; Hu, H. L.; Khor, K. A.; Wang, Y.; Dong, Z. L. Microstructure and Strengthening Mechanisms in the Al/Al−Cu−Cr−Fe Composites Consolidated Using Spark Plasma Sintering. *Mater. Charact.* **2019**, *157*, 109917.

(8) Lowe, M.; Yadav, T. P.; Fournée, V.; Ledieu, J.; McGrath, R.; Sharma, H. R. Influence of Leaching on Surface Composition, Microstructure, and Valence Band of Single Grain Icosahedral Al-Cu-Fe Quasicrystal. *J. Chem. Phys.* **2015**, *142*, 104702.
(9) Hou, Z.; Hua, M.; Liu, Y.; Deng, J.; Zhou, X.; Feng, Y.; Li, Y.; Dai, H. Exploring Intermetallic Compounds: Properties and Applications in Catalysis. *Catalysts* **2024**, *14*, 538.
(10) Verma, S. K.; Bhatnagar, A.; Shaz, M. A.; Yadav, T. P. Mechanistic Understanding of the Superior Catalytic Effect of $Al_{65}Cu_{20}Fe_{15}$ Quasicrystal on De/Re-Hydrogenation of $NaAlH_4$. *Int. J. Hydrogen Energy* **2023**, *48*, 9762−9775.
(11) Azuha, A. A.; Klimkowicz, A.; Takasaki, A. Quaternary Quasicrystal Alloys for Hydrogen Storage Technology. *MRS Adv.* **2020**, *5*, 1071−1083.
(12) Tsai, A. P.; Yoshimura, M. Highly Active Quasicrystalline Al-Cu-Fe Catalyst for Steam Reforming of Methanol. *Appl. Catal., A* **2001**, *214*, 237−241.
(13) Tanabe, T.; Kameoka, S.; Tsai, A. P. Microstructure of Leached Al-Cu-Fe Quasicrystal with High Catalytic Performance for Steam Reforming of Methanol. *Appl. Catal., A* **2010**, *384*, 241−251.
(14) Ngoc, B.; Geantet, C.; Aouine, M.; Bergeret, G.; Raffy, S.; Marlin, S. Quasicrystal Derived Catalyst for Steam Reforming of Methanol. *Int. J. Hydrogen Energy* **2008**, *33*, 1000−1007.
(15) Tanabe, T.; Kameoka, S.; Tsai, A. P. Evolution of Microstructure Induced by Calcination in Leached Al−Cu−Fe Quasicrystal and Its Effects on Catalytic Activity. *J. Mater. Sci.* **2011**, *46*, 2242−2250.
(16) Tanabe, T.; Kameoka, S.; Tsai, A. P. A Novel Catalyst Fabricated from Al−Cu−Fe Quasicrystal for Steam Reforming of Methanol. *Catal. Today* **2006**, *111*, 153−157.
(17) Mishra, S. S.; Yadav, T. P.; Singh, S. P.; Singh, A. K.; Shaz, M. A.; Mukhopadhyay, N. K.; Srivastava, O. N. Evolution of Porous Structure on Al−Cu−Fe Quasicrystalline Alloy Surface and Its Catalytic Activities. *J. Alloys Compd.* **2020**, *834*, 155162.
(18) Pandey, S. K.; Bhatnagar, A.; Mishra, S. S.; Yadav, T. P.; Shaz, M. A.; Srivastava, O. N. Curious Catalytic Characteristics of Al-Cu-Fe Quasicrystal for De/Rehydrogenation of MgH_2. *J. Phys. Chem. C* **2017**, *121*, 24936−24944.
(19) Mishra, S. S.; Yadav, T. P.; Mukhopadhyay, N. K.; Srivastava, O. N. Synthesis of Fine Skeletal Structure on Al−Cu−Co Decagonal Quasicrystals for Hydrogen Production through Steam Reforming of Methanol. *Int. J. Hydrogen Energy* **2020**, *45*, 24491−24501.
(20) Wolf, W.; Bolfarini, C.; Kiminami, C. S.; Botta, W. J. Fabrication of Al-Matrix Composite Reinforced with Quasicrystals Using Conventional Metallurgical Fabrication Methods. *Scr. Mater.* **2019**, *173*, 21−25.
(21) Oladoye, P. O.; Bamigboye, M. O.; Ogunbiyi, O. D.; Akano, M. T. Toxicity and Decontamination Strategies of Congo Red Dye. *Groundw. Sustain. Dev.* **2022**, *19*, 100844.
(22) Mazzer, E. M.; Afonso, C. R. M.; Galano, M.; Kiminami, C. S.; Bolfarini, C. Microstructure Evolution and Mechanical Properties of Al−Zn−Mg−Cu Alloy Reprocessed by Spray-Forming and Heat Treated at Peak Aged Condition. *J. Alloys Compd.* **2013**, *579*, 169−173.
(23) Naseem, K.; Farooqi, Z. H.; Begum, R.; Irfan, A. Removal of Congo Red Dye from Aqueous Medium by Its Catalytic Reduction Using Sodium Borohydride in the Presence of Various Inorganic Nano-Catalysts: A Review. *J. Cleaner Prod.* **2018**, *187*, 296−307.
(24) Bhat, S. S. M.; Sundaram, N. G. Efficient Visible Light Photocatalysis of Bi_4TaO_8Cl Nanoparticles Synthesized by Solution Combustion Technique. *RSC Adv.* **2013**, *3*, 14371−14378.
(25) Wang, L.; Li, J.; Wang, Z.; Zhao, L.; Jiang, Q. Low-Temperature Hydrothermal Synthesis of α-Fe/Fe_3O_4 Nanocomposite for Fast Congo Red Removal. *Dalton Trans.* **2013**, *42*, 2572−2579.
(26) Hu, C.; Chen, Z.; Shen, A.; Shen, X.; Li, J.; Hu, S. Water-Soluble single-Walled Carbon Nanotubes Via Noncovalent Functionalization By a Rigid, Planar And Conjugated Diazo Dye. *Carbon* **2006**, *44*, 428−434.
(27) Glover, J. R.; Thomas, B. M. Case Report: Severe Adverse Reaction to Oral Iohexol. *Clin. Radiol.* **1991**, *44*, 137−138.
(28) Wolf, W.; e Silva, L. P. M.; Zepon, G.; Kiminami, C. S.; Bolfarini, C.; Botta, W. J. Single Step Fabrication by Spray Forming of Large Volume Al-Based Composites Reinforced with Quasicrystals. *Scr. Mater.* **2020**, *181*, 86−91.
(29) Mishra, S. S.; Yadav, T. P.; Mukhopadhyay, N. K.; Srivastava, O. N. Leaching of Rapidly Quenched $Al_{65}Cu_{20}Fe_{15}$ Quasicrystalline Ribbons. *Bull. Mater. Sci.* **2017**, *40*, 1529−1533.
(30) Ura-Binczyk, E.; Homazava, N.; Ulrich, A.; Hauert, R.; Lewandowska, M.; Kurzydlowski, K. J.; Schmutz, P. Passivation of Al−Cr−Fe and Al−Cu−Fe−Cr Complex Metallic Alloys in 1 M H_2SO_4 and 1 M NaOH Solutions. *Corros. Sci.* **2011**, *53*, 1825−1837.
(31) Yadav, T. P.; Mishra, S. S.; Pandey, S. K.; Singh, D.; Lowe, M.; Tamura, R.; Mukhopadhyay, N. K.; Srivastava, O. N.; McGrath, R.; Sharma, H. R. Leaching of Al-Based Polygrain Quasicrystalline and Related Crystalline Surfaces. *Acta Phys. Pol., A* **2014**, *126*, 629−632.
(32) Qian, D.; Xu, B.; Chi, M.; Meng, Y. S. Uncovering the Roles of Oxygen Vacancies in Cation Migration in Lithium Excess Layered Oxides. *Phys. Chem. Chem. Phys.* **2014**, *16*, 14665−14668.
(33) D'Angelo, D.; Bongiorno, C.; Amato, M.; Deretzis, I.; La Magna, A.; Compagnini, G.; Spanò, S. F.; Scalese, S. Electron energy-Loss Spectra Of Graphene Oxide For The Determination Of Oxygen Functionalities. *Carbon* **2015**, *93*, 1034−1041.
(34) Riegler, K.; Kothleitner, G. EELS Detection Limits Revisited: Ruby — A Case Study. *Ultramicroscopy* **2010**, *110*, 1004−1013.
(35) Leapman, R. D.; Grunes, L. A.; Fejes, P. L. Study of the L_{23} Edges in the 3d Transition Metals and Their Oxides by Electron-Energy-Loss Spectroscopy with Comparisons to Theory. *Phys. Rev. B* **1982**, *26*, 614−635.
(36) Rosenberger, T.; Skenderović, I.; Sellmann, J.; Wollny, P.; Levish, A.; Wlokas, I.; Kempf, A.; Winterer, M.; Kruis, F. E. Determining the Sintering Kinetics of Fe and Fe_xO_y-Nanoparticles in a Well-Defined Model Flow Reactor. *Aerosol Sci. Technol.* **2022**, *56*, 833−846.
(37) Walls, M. G.; Cao, C.; Yu-Zhang, K.; Li, J.; Che, R.; Pan, Y. Identification of Ferrous-Ferric Fe_3O_4 Nanoparticles in Recombinant Human Ferritin Cages. *Microsc. Microanal.* **2013**, *19*, 835−841.
(38) Cavalca, F.; Laursen, A. B.; Wagner, J. B.; Damsgaard, C. D.; Chorkendorff, I.; Hansen, T. W. Light-Induced Reduction of Cuprous Oxide in an Environmental Transmission Electron Microscope. *ChemCatchem* **2013**, *5*, 2667−2672.
(39) Hulbert, S. L.; Bunker, B. A.; Brown, F. C.; Pianetta, P. Copper $L_{2,3}$ Near-Edge Structure in Cu_2O. *Phys. Rev. B* **1984**, *30*, 2120−2126.
(40) Ngantcha, J. P.; Gerland, M.; Kihn, Y.; Riviére, A. Correlation between Microstructure and Mechanical Spectroscopy of a Cu−Cu_2O Alloy between 290 and 873 K. *Eur. Phys. J. Appl. Phys.* **2005**, *29*, 83−89.
(41) Sing, K. S. W. Reporting Physisorption Data for Gas/Solid Systems with Special Reference to the Determination of Surface Area and Porosity. *Pure Appl. Chem.* **1982**, *54* (11), 2201−2218.
(42) Kamal, T.; Khan, S. B.; Asiri, A. M. Synthesis of Zero-Valent Cu Nanoparticles in the Chitosan Coating Layer on Cellulose Microfibers: Evaluation of Azo Dyes Catalytic Reduction. *Cellulose* **2016**, *23*, 1911−1923.
(43) Muedi, K. L.; Masindi, V.; Maree, J. P.; Brink, H. G. Rapid Removal of Cr(VI) from Aqueous Solution Using Polycationic/Di-Metallic Adsorbent Synthesized Using Fe^{3+}/Al^{3+} Recovered from Real Acid Mine Drainage. *Minerals* **2022**, *12*, 1318.
(44) Sun, X.; Liu, Z.; Zheng, Z.; Yu, H.; Zeng, D. Improved Adsorption of Congo Red by Nanostructured Flower-like Fe(II)−Fe(III) Hydroxy Complex. *Water Sci. Technol.* **2018**, *78*, 506−514.
(45) Huang, L.-Y.; Li, W.; Du, N.; Lu, H.-Q.; Meng, L.-D.; Huang, K.-Y.; Li, K. Preparation of Quaternary Ammonium Magnetic Chitosan Microspheres and Their Application for Congo Red Adsorption. *Carbohydr. Polym.* **2022**, *297*, 119995.
(46) Muedi, K.; Masindi, V.; Maree, J.; Haneklaus, N.; Brink, H. Effective Adsorption of Congo Red from Aqueous Solution Using Fe/Al Di-Metal Nanostructured Composite Synthesised from Fe(III) and

Al(III) Recovered from Real Acid Mine Drainage. *Nanomaterials* **2022**, *12*, 776.
(47) Narasaiah, B. P.; Mandal, B. K. Remediation of Azo-Dyes Based Toxicity by Agro-Waste Cotton Boll Peels Mediated Palladium Nanoparticles. *J. Saudi Chem. Soc.* **2020**, *24*, 267−281.
(48) Ismail, M.; Gul, S.; Khan, M. I.; Khan, M. A.; Asiri, A. M.; Khan, S. B. Green Synthesis of Zerovalent Copper Nanoparticles for Efficient Reduction of Toxic Azo Dyes Congo Red and Methyl Orange. *Green Process. Synth.* **2019**, *8*, 135−143.
(49) Rajesh, R.; Kumar, S. S.; Venkatesan, R. Efficient Degradation of Azo Dyes Using Ag and Au Nanoparticles Stabilized on Graphene Oxide Functionalized with PAMAM Dendrimers. *New J. Chem.* **2014**, *38*, 1551−1557.
(50) Chen, M.; Liu, P.; Wang, C.; Ren, W.; Diao, G. Fast Catalytic Reduction of an Azo Dye by Recoverable and Reusable Fe_3O_4@PANI@Au Magnetic Composites. *New J. Chem.* **2014**, *38*, 4566−4573.
(51) Liu, X.; Liang, M.; Liu, M.; Su, R.; Wang, M.; Qi, W.; He, Z. Highly Efficient Catalysis of Azo Dyes Using Recyclable Silver Nanoparticles Immobilized on Tannic Acid-Grafted Eggshell Membrane. *Nanoscale Res. Lett.* **2016**, *11*, 440.
(52) Ghosh, B. K.; Hazra, S.; Naik, B.; Ghosh, N. N. Preparation of Cu Nanoparticle Loaded SBA-15 and Their Excellent Catalytic Activity in Reduction of Variety of Dyes. *Powder Technol.* **2015**, *269*, 371−378.
(53) Wang, L.; Wang, A. Adsorption Properties of Congo Red from Aqueous Solution onto Surfactant-Modified Montmorillonite. *J. Hazard. Mater.* **2008**, *160*, 173−180.
(54) Moon, S. A.; Salunke, B. K.; Saha, P.; Deshmukh, A. R.; Kim, B. S. Comparison of Dye Degradation Potential of Biosynthesized Copper Oxide, Manganese Dioxide, and Silver Nanoparticles Using *Kalopanax pictus*. *Plant Extract. Korean J. Chem. Eng.* **2018**, *35*, 702−708.
(55) Kalwar, N. H.; Sirajuddin; Sherazi, S. T. H.; Khaskheli, A. R.; Hallam, K. R.; Scott, T. B.; Tagar, Z. A.; Hassan, S. S.; Soomro, R. A. Fabrication of Small L-Threonine Capped Nickel Nanoparticles and Their Catalytic Application. *Appl. Catal., A* **2013**, *453*, 54−59.
(56) Gupta, S.; Giordano, C.; Gradzielski, M.; Mehta, S. K. Microwave-Assisted Synthesis of Small Ru Nanoparticles and Their Role in Degradation of Congo Red. *J. Colloid Interface Sci.* **2013**, *411*, 173−181.
(57) Atarod, M.; Nasrollahzadeh, M.; Sajadi, S. M. Euphorbia *heterophylla* Leaf Extract Mediated Green Synthesis of Ag/TiO_2 Nanocomposite and Investigation of Its Excellent Catalytic Activity for Reduction of Variety of Dyes in Water. *J. Colloid Interface Sci.* **2016**, *462*, 272−279.
(58) Zheng, Y.; Wang, A. Ag Nanoparticle-Entrapped Hydrogel as Promising Material for Catalytic Reduction of Organic Dyes. *J. Mater. Chem.* **2012**, *22*, 16552−16559.

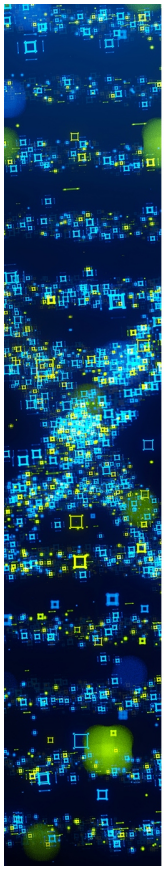
CAS BIOFINDER DISCOVERY PLATFORM™
STOP DIGGING THROUGH DATA —START MAKING DISCOVERIES
CAS BioFinder helps you find the right biological insights in seconds
Start your search
CAS
A division of the American Chemical Society

https://doi.org/10.1021/acs.jpcc.5c03000
J. Phys. Chem. C 2025, 129, 14366−14377